Energy 228 (2021) 120494

Contents lists available at ScienceDirect

Energy

journal homepage: www.elsevier.com/locate/energy

Superheater deposits and corrosion in temperature gradient – Laboratory studies into effects of flue gas composition, initial deposit structure, and exposure time

Jonne Niemi [a, *], Markus Engblom [b], Tor Laurén [b], Patrik Yrjas [b], Juho Lehmusto [b], Mikko Hupa [b], Daniel Lindberg [a]

[a] Aalto University School of Chemical Engineering, Department of Chemical and Metallurgical Engineering, Kemistintie 1, P.O. Box 16100, FI-00076 Aalto, Espoo, Finland
[b] Johan Gadolin Process Chemistry Centre, C/o Laboratory of Molecular Science and Engineering, Åbo Akademi University, Biskopsgatan 8, FI-20500, Åbo/Turku, Finland

ARTICLE INFO

Article history:
Received 12 February 2021
Received in revised form
23 March 2021
Accepted 26 March 2021
Available online 29 March 2021

Keywords:
Temperature gradient
High-temperature corrosion
Sulfation
Alkali chlorides
Ash deposits

ABSTRACT

The heterogeneous nature of the ash chemistry of biomass fuels gives rise to challenges in predicting the deposit melting, sintering, and enrichment of corrosive ash species. An experimental method has been developed to study the evolution of ash deposit chemistry and morphology in temperature gradients simulating the conditions of real superheater deposits. The method is based on applying synthetic ash mixtures on an air-cooled corrosion probe, which is inserted into a tube furnace. The focus has been on how the melting behavior of alkali salt-rich deposits, i.e., $KCl–K_2SO_4–NaCl–Na_2SO_4$ mixtures, affects the chemistry and morphology. Intradeposit vaporization-condensation of alkali chlorides has been of interest. The interaction of reactive gas components ($H_2O + SO_2$), with the deposits, was also studied. The vaporization-condensation mechanism leads to enrichment of alkali chlorides in crevices and voids within deposits, leading also to build-up of chlorides on the steel surface, which causes accelerated corrosion, due to the formation of low-melting $FeCl_2$ mixtures. Liquid phase sintering and temperature gradient zone melting (TGZM) were the main mechanisms for the supersolidus sintering of the deposits. Iron and nickel oxides were found within the deposits and at the outer edge of deposits, due to the TGZM mechanism.

1. Introduction

Fuel ash in steam boilers can form deposits on heat exchanger surfaces. Heat exchanger deposits can lead to a range of challenges during boiler operation, e.g. by inducing corrosion or by plugging the flue gas path, especially in boilers firing biomass and waste [1]. Heat exchanger deposits are generally heterogeneous in both composition and morphology. The heterogeneous nature is due to the combined effects of the deposit formation mechanisms (i.e., condensation, thermophoresis, eddy impaction, and inertial impaction) and changes occurring in the deposit after the deposit formation. These changes can be induced both by internal mechanisms, i.e., changes occurring due to the nature of the deposit and normal steady-state conditions, as well as by external mechanisms, i.e., caused by phenomena such as soot-blowing. Deposit shedding may be due to both types of phenomena [2].

The temperature difference between the hot flue gas and the colder heat exchanger surface results in a temperature gradient over the ash deposit. The effect of the temperature gradient has been considered in many corrosion and laboratory-scale deposit studies [3–13]. The temperature gradient studies have shown that the furnace/atmosphere temperature affects corrosion. The higher temperature in the atmosphere, i.e. steeper temperature gradient from the furnace temperature to the steel sample, results in faster corrosion although the steel temperature is the same [3,13,14]. In addition, changing the temperature profile in thermal cycles has been shown to deteriorate the protective oxide layer and induce faster corrosion [5].

Several of the studies have been conducted at Åbo Akademi University by utilizing a cooled laboratory-scale probe with

* Corresponding author.
E-mail address: jonne.niemi@aalto.fi (J. Niemi).

https://doi.org/10.1016/j.energy.2021.120494

Table 1
Earlier conducted temperature gradient deposit and corrosion experiments.

Synthetic deposit/Salt system	Steel temperature, °C	Steel grade	Exposure time, h	Reference
$NaCl-Na_2SO_4$	300, 400, 500	10CrMo9-10	4–72	[7,10]
$KCl-K_2SO_4$	300, 400, 500	10CrMo9-10	4–72	[7,10]
$NaBr-Na_2SO_4$	500	10CrMo9-10, P235GH	2–8	[8]
$KBr-K_2SO_4$	500	10CrMo9-10, P235GH	2–8	[8]
$PbCl_2-SiO_2$	200, 400	P235GH	4–24	[11]
$NaCl-PbCl_2$	400	P235GH	4–24	[11]
$Na_2SO_4-PbCl_2$	200, 400	P235GH	24	[11]
$KCl-PbCl_2$	200, 400	P235GH	24	[11]
$K_2SO_4-PbCl_2$	200, 305, 400	P235GH	24	[11,12]
$KCl-NaCl-PbCl_2$	200, 400	P235GH	24	[11]

removable steel sample rings covered with a deposit material [7,8,10–12]. In the studies, the cooled probe was placed in a hot tube furnace thus producing a temperature gradient across the deposit material. The studies were focused on deposit chemistry and high-temperature corrosion. The studied parameters are summarized in Table 1. All experiments published so far have been conducted with the same grain size deposits (53–250 μm) and in an ambient atmosphere.

The mechanisms that have been observed to affect the deposit morphology and chemistry are: i) liquid phase sintering, ii) temperature gradient zone melting, and iii) vaporization-condensation of volatile species [7,8,10].

The morphological changes in the deposits exposed to temperature gradients occur mainly due to melt formation. Formation of melt induces liquid phase sintering in initially porous deposits. The resulting deposit structures are either dense structures or network-like structures depending on the melt amount present [7,11]. In addition to structural changes, the local deposit composition was observed to be affected by the liquid phase sintering mechanism. The components incorporated in the melt phase enriched at the location with the temperature corresponding to the solidus temperature of the composition in question.

Temperature gradient zone melting affects the supersolidus regions of deposits. When a solid-liquid system, where the liquid is surrounded by its primary crystallizing phase and the liquid phase composition is a function of the temperature, is subjected to a temperature gradient, a concentration gradient develops in the liquid phase. A simple example of such a system is a eutectic binary system. The concentration gradient results in species diffusion within the liquid phase, which results in further melting in the hotter part and solidification in the colder part of the considered system. The overall mechanism results in a liquid phase movement towards the hotter temperature. Temperature gradient zone melting has been observed to affect the deposit chemistry in both the binary (e.g. $NaCl-Na_2SO_4$) [7,8] and higher-order (e.g. $KCl-NaCl-K_2SO_4-Na_2SO_4$) [9] systems.

Vaporization-condensation of volatile species has been shown to result in enrichment of corrosive alkali halide species towards the cooled steel. The mechanism responsible for the alkali halide transport has been identified to be temperature gradient-induced concentration diffusion within the gas phase [7,8,10].

Gaseous $PbCl_2$ has been shown to condense from the surrounding furnace gas atmosphere into the porous salt deposits. The interactions between the $PbCl_2$ and the salt deposits (KCl, K_2SO_4, NaCl, Na_2SO_4) were shown to result in chemical reactions between the salts, melting of deposits, and enrichment of Pb and Cl containing species towards the cooled steel surface [11]. With NaCl and $PbCl_2$, the interaction was a formation of a eutectic melt. No chemical reactions were observed between NaCl and $PbCl_2$, as no mixed solid Na–Pb–Cl compounds are known to exist. With Na_2SO_4, K_2SO_4, and KCl, in addition to the formation of molten phases, the $PbCl_2$ was observed to also react and form new compounds (K_2PbCl_4, $K_3Pb_2(SO_4)_3Cl$, and $Na_3Pb_2(SO_4)_3Cl$).

The observed phenomena occurring in ash deposits exposed to temperature gradients are summarized in Fig. 1.

The objective of this study is to extend the understanding of how different parameters affect ash deposit aging and superheater corrosion in the presence of temperature gradients. The studied parameters are i) the effect of gas phase composition, i.e., ambient atmosphere vs. humid atmosphere vs. humid atmosphere with SO_2, ii) the effect of longer exposure times, i.e., 168 h compared to earlier 2–72 h, and iii) the effect of deposit particle size, i.e., 30–53 μm particles compared to earlier tested 53–250 μm particles. The aim is to gain a more comprehensive understanding of the fundamental phenomena taking place in boiler ash deposits in temperature gradients, how deposits interact with flue gases, and how these phenomena affect the corrosion behavior of superheater materials.

2. Experimental

The main experimental setup consists of a laboratory-scale air-cooled probe, which is inserted into a tube furnace. Synthetic ash deposits are applied on top of changeable steel rings, which are a part of the probe. The furnace temperature is higher (~800 °C) than the probe temperature (~500 °C), creating a temperature gradient over the few mm thick deposit. The temperature gradient simulates a real boiler situation where a temperature gradient is present over the deposit, from the flue gas to the steel. A detailed description of the setup can be found from our previous studies [7,10].

The flue gas temperature in the superheater region varies between boilers. In addition, the temperature decreases from the inlet to the outlet of the superheater region as heat is transferred from the flue gas to the steam. The flue gas temperature is typically 800–1200 °C in the superheater region and is lowered to 400–600 °C after the superheater region [15,16]. The furnace atmosphere temperature in the laboratory experiments (800 °C) was chosen so that it is representative of a boiler flue gas temperature in the superheater region. The probe temperature (500 °C) was chosen so that it is representative of a superheater material temperature in a biomass-fired boiler [15,17] or a black liquor recovery boiler [18,19].

The steel sample rings were made from commercial steel grades, either 10CrMo9-10 or Sanicro 28, and their compositions are listed in Table 2. 10CrMo9-10 is a low alloy ferritic steel and Sanicro 28 is an austenitic stainless steel. The steel grades were chosen as they are typical superheater materials.

The steel sample rings each house a thermocouple, one of which is connected to a PID-regulator that controls a valve, which regulates the flow of the cooling air into the probe and thus the temperature of the probe. The other thermocouple is used to measure and record the temperature during experiments. During experiments, the sample rings had usually a temperature difference of

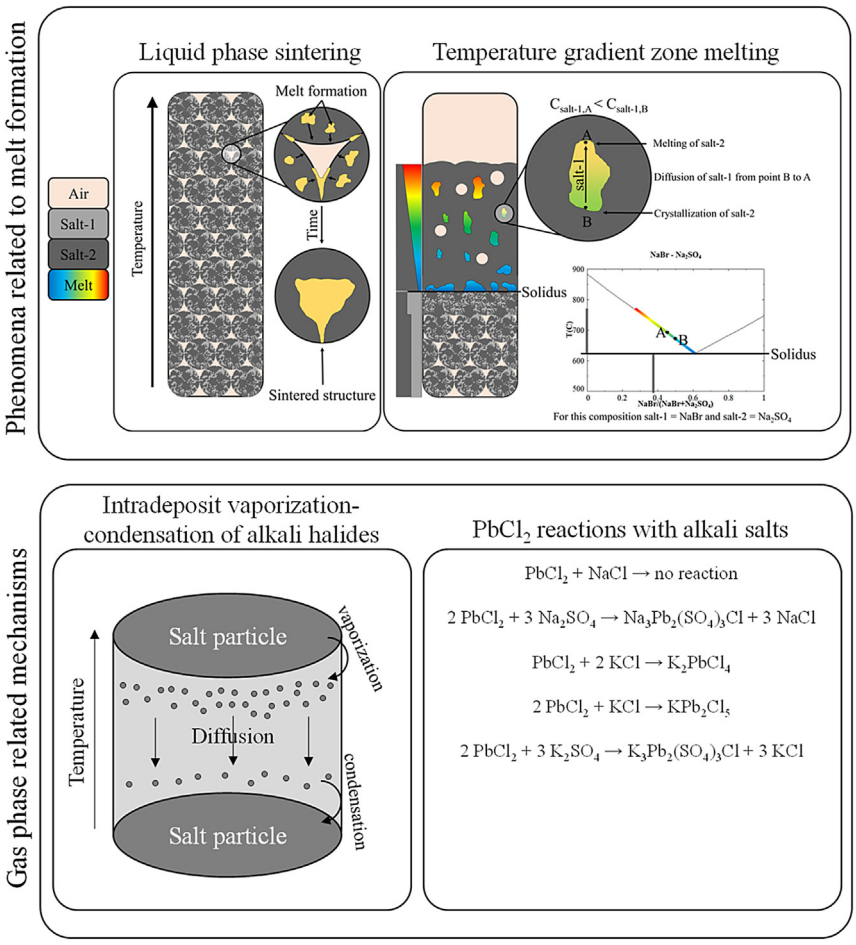

Fig. 1. Summary of the temperature gradient induced effects in laboratory experiments [7,8,10,11].

Table 2
Nominal and SEM/EDS measured (in the parenthesis) compositions of the tested steels in wt-%.

Steel	Cr	Cu	Fe	Mn	Mo	Ni	Si
10CrMo9-10	2.3 (2.3)	–	93.4 (95.8)	0.8 (0.6)	1.0 (0.9)	–	0.3 (0.3)
Sanicro 28	25.9 (27.0)	1.2 (0.9)	35.9 (36.7)	2.0 (1.9)	3.4 (3.2)	29.2 (29.7)	0.2 (0.6)

approximately 10 °C, as can be seen from Table 3. One additional thermocouple was placed above the deposits to measure and record the temperature of the furnace atmosphere during the exposure. Table 3 summarizes the conducted experiments discussed in this paper.

The deposit materials applied on top of the steel sample rings were salt mixtures, which were homogenized before the experiment. The homogenization was conducted by melting the salt mixture in question, crushing it, and sieving it to the desired size fraction. When a single component salt (e.g., NaCl) was used as deposit material, the salt was only crushed and sieved.

The deposit constituents were chosen due to them being common in superheater deposits. Alkali chloride-induced high-temperature corrosion is one of the main reasons limiting steam temperatures in biomass and waste-fired boilers [15]. The potassium salt mixtures are relevant for biomass ash deposits, e.g. in straw-fired boilers [15,20,21]. The sodium salt mixtures in their turn are relevant for black liquor recovery boilers [19] or waste-fired boilers [22].

The effects of different gas atmospheres were studied with NaCl and KCl (53–250 μm). These two salts were studied in ambient, humid (20% H_2O + 80% air), and humid with SO_2 (20% H_2O + 80% air + 100 ppm SO_2) atmospheres, with a steel temperature adjusted to 500 °C for 24 h. The chosen H_2O content of 20% in the atmosphere is high and corresponds e.g., to a flue gas composition from the combustion of fuel with ~50 wt% moisture, fired with an air ratio of ~1.3 [23]. The chosen SO_2 content of 100 ppm is similar as has been measured in the flue gas of co-fired straw pellets and peat [24].

The humid air feed was first circulated in another furnace (preheater) at 200 °C. The humid air was fed to the furnace with the probe from the preheater. When SO_2 was added to the atmosphere, it also passed through the preheater. There was a constant flow of air through the furnace, to keep the conditions at a steady state. A flow rate of 2.4 normal liters/min was used.

After each furnace exposure, the sample rings along with the deposits were detached from the probe and cast in epoxy resin. The samples were cut for a cross-section and analyzed with SEM/EDX. In addition, the salt melting properties and melt compositions were estimated with thermodynamic calculations. The thermodynamic calculations were conducted with FactSage 7.3 software, using the FTsalt database [25].

Table 3
The conducted experiments with the experimental parameters. Furnace temperature = 800 °C.

Steel	Steel temperature [°C]	Exposure time [h]	Salt composition [wt-%]				Salt particle size [μm]	Atmosphere
			NaCl	Na_2SO_4	KCl	K_2SO_4		
10CrMo9-10	500	4			11	89	30–53	air
Sanicro 28	512	4			11	89	30–53	air
10CrMo9-10	500	4	6	94			30–53	air
Sanicro 28	512	4	6	94			30–53	air
10CrMo9-10	500	24			11	89	30–53	air
Sanicro 28	515	24			11	89	30–53	air
10CrMo9-10	500	24			91	9	30–53	air
Sanicro 28	515	24			91	9	30–53	air
10CrMo9-10	500	24			55	45	30–53	air
Sanicro 28	513	24			55	45	30–53	air
10CrMo9-10	500	24	6	94			30–53	air
Sanicro 28	512	24	6	94			30–53	air
10CrMo9-10	500	24	87	13			30–53	air
Sanicro 28	515	24	87	13			30–53	air
10CrMo9-10	500	24	32	68			30–53	air
Sanicro 28	512	24	32	68			30–53	air
10CrMo9-10	500	24			100		53–250	air
10CrMo9-10	500	24			100		53–250	20% H_2O + 80% air
10CrMo9-10	500	24			100		53–250	20% H_2O + 80% air + 100 ppm SO_2
10CrMo9-10	510	24	100				53–250	air
10CrMo9-10	500	24	100				53–250	20% H_2O + 80% air
10CrMo9-10	500	24	100				53–250	20% H_2O + 80% air + 100 ppm SO_2
Sanicro 28	500	24	100				53–250	air
Sanicro 28	504	24	100				53–250	20% H_2O + 80% air
Sanicro 28	508	24			100		53–250	20% H_2O + 80% air
10CrMo9-10	500	168			55	45	53–250	air
10CrMo9-10	500	168	55	45			53–250	air
Sanicro 28	511	168			55	45	53–250	air
Sanicro 28	517	168	55	45			53–250	air

3. Results and Discussion

3.1. Effect of particle size

The deposits with a 30–53 μm particle size formed multilayered morphologies during the furnace treatment. The outer region of the deposits, facing the hot furnace atmosphere and experiencing hotter temperatures sintered and formed dense structures. Closer to the cooled steel, the deposit particles were observed as discrete particles and to have retained their sharp edges. Examples of typical deposit morphologies are shown in Figs. 2 and 3.

The discrete region formation has earlier been concluded to occur due to the partial melting of the deposit [7,10]. Similar, though more complex, multilayered deposit morphologies have been observed in straw-fired boilers [20,26,27]. In the laboratory experiments, the interface between the outer and the inner layer (see Figs. 2 and 3) was considered to have been at the location where the temperature corresponds to the first melting temperature of the deposit material in question, 626 °C for $NaCl–Na_2SO_4$ and 690 °C for $KCl–K_2SO_4$. The sharp interface is connected to the liquid phase movement due to the temperature gradient zone melting phenomenon [7].

Above the first melting temperature, sintering was observed to occur at a high degree with the 30–53 μm particles compared to earlier published 53–250 μm particles results [7,10]. The earlier studied 53–250 μm particle deposits with $KCl–K_2SO_4$ 11:89 wt-% composition had a network structure [7,10]. The 30–53 μm particle deposits with the same composition were observed to sinter more, forming denser morphologies with less porosity than the 53–250 μm particle deposits, as shown in Fig. 3.

The smaller particles have a higher surface-area-to-volume ratio, which makes them more prone to sintering via liquid phase sintering [28]. However, the only composition where the particle size seemed to matter was the $KCl–K_2SO_4$ 11:89 wt-% mixture. With the other salt compositions, the sintering of the deposits above the solidus temperature resulted in dense deposit structures with both the small and large particle size deposits. With the $KCl–K_2SO_4$ 11:89 wt-% mixture, the 30–53 μm particle size deposits had a dense structure above the solidus temperature and the 53–250 μm particle size deposits had a network structure.

The tested compositions were chosen so that the melt present at the first melting temperature was either 20 or 100 wt-%. Even so, the melting behavior and the share of melt at 800 °C (the furnace temperature) are different depending on the chemical composition (Fig. 4). The share of melt for the $KCl–K_2SO_4$ 11:89 wt-% composition at 800 °C is 31 wt-%, while the other tested compositions at the same temperature have over 75 wt-% molten phase. With a high share of molten phase present, the effect of the surface-area-to-volume ratio becomes negligible as most of the deposit is in the liquid phase. With lower shares of molten phase, the surface-area-to-volume ratio strongly affects the sintering and densification of the deposit material, hence the difference between the 30–53 μm and 53–250 μm particle size results with the $KCl–K_2SO_4$ 11:89 wt-% composition (as seen in Figs. 2 and 3).

An implication of the impact of the share of melt present is that deposit sintering in actual boiler deposits can be expected to depend on the deposit chlorine content. More work is needed to understand better the impact of the deposit melting behavior on deposit sintering. However, it is currently known that the chlorine content of black liquor recovery boiler fly ash varies typically in the range 1–10 wt-% [29]. In addition, preliminary data from recovery boilers indicates that deposits have a network structure at lower chlorine content, while the structure is dense at higher chlorine content [18,29].

The enrichment of the molten phase constituents towards the cooled steel surface and subsequent hardening of deposits has been also reported by Laxminarayan et al. [30]. They report that a formation and subsequent movement of melt affects the removability

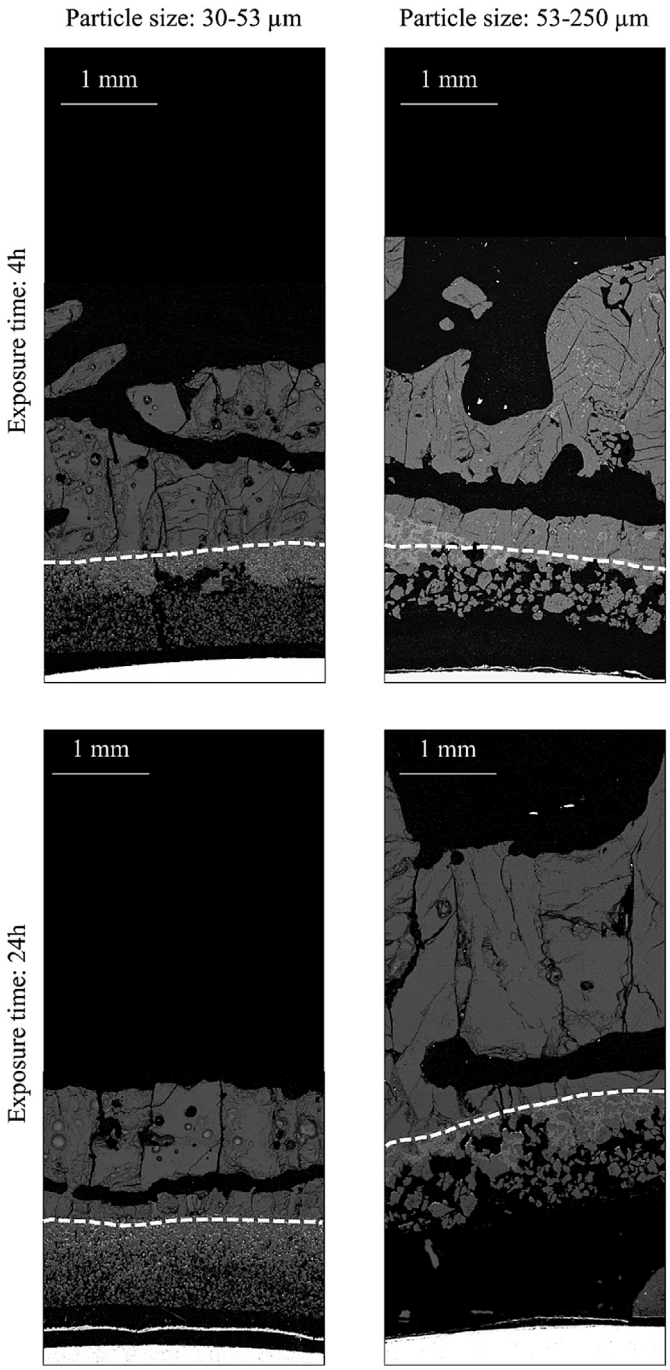

Fig. 2. SEM backscatter electron images displaying typical deposit morphologies of NaCl–Na_2SO_4 (6:94 wt-%) deposits with 4 h (upper row) and 24 h (lower row) exposure times with 30–53 μm (left column) and 53–250 μm [7] (right column) particle sizes, with the steel temperature at 500 °C. In the images: black = epoxy, darker grey = Na_2SO_4, lighter grey = NaCl, and light at the bottom = steel/oxide. The interfaces between the outer and the inner layers are indicated in the Figure with dashed white lines.

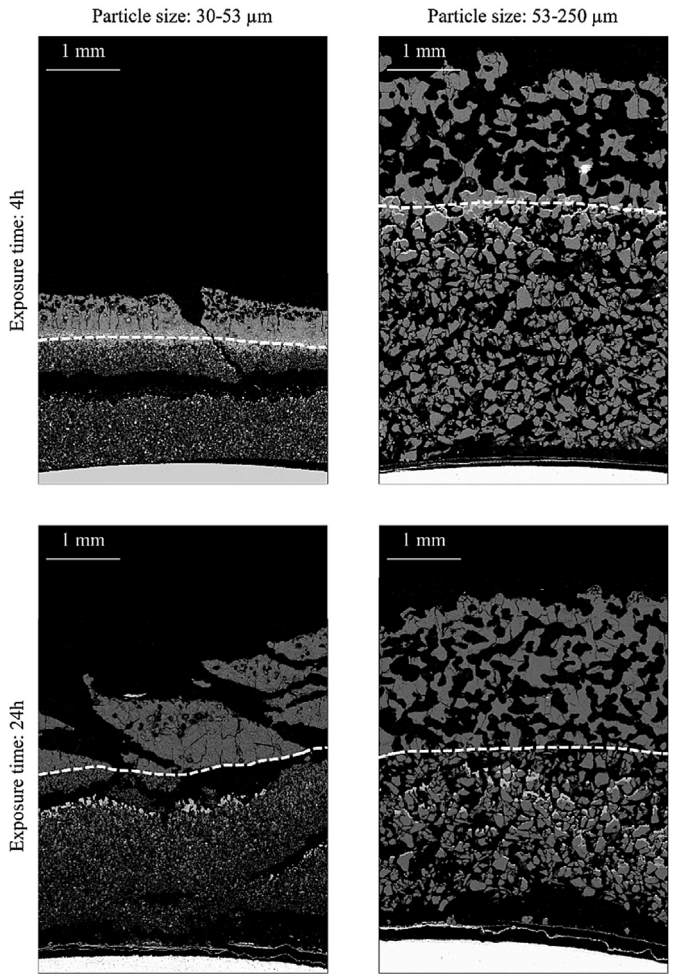

Fig. 3. SEM backscatter electron images displaying typical deposit morphologies of KCl–K_2SO_4 (11:89 wt-%) deposits with 4 h (upper row) and 24 h (lower row) exposure times with 30–53 μm (left column) and 53–250 μm [7] (right column) particle sizes, with the steel temperature at 500 °C. In the images: black = epoxy, darker grey = K_2SO_4, lighter grey = KCl, and light at the bottom = steel/oxide. The interfaces between the outer and the inner layers are indicated in the Figure with dashed white lines.

of deposits by increasing the adhesion strength of deposits to the heat exchanger surfaces. Compared to the larger particle deposits, the smaller particle deposits sintered more. The implication is that deposits consisting of finer particles are more prone to sintering and deposit densification, which could make them harder to remove.

Pure alkali chloride layers were observed on the furnace-facing sides and alkali chloride void areas were observed on the steel-facing sides of the deposit particles. The thicknesses of these alkali chloride layers as a function of temperature were quantified from the SEM images as described by Lindberg et al. [10]. The thicknesses of the layers and the distances of the layers from the steel surface were measured from the SEM images. The distances from the steel surface were converted to estimated local temperatures within the deposits, by using the bulk temperature gradient values over the porous part of the deposits [10]. Generally, the KCl layers were observed to be thicker than the NaCl layers, which is mainly due to the difference in the partial pressures of KCl and NaCl species [7,10].

The 30–53 μm particle deposits mostly had thinner alkali chloride layers than the 53–250 μm particle deposits. In addition, the thickest alkali chloride layers in 30–53 μm deposits were observed in cracks or larger crevices within the deposits, and the region above a crack was always devoid of alkali chlorides (see Fig. 5). Fig. 6 shows the thicknesses of the deposit alkali chloride layers. Thicknesses of the thicker alkali chloride layers, grown into the cracks, are shown separately.

In the experiments with 53–250 μm particles, similar cracks, as

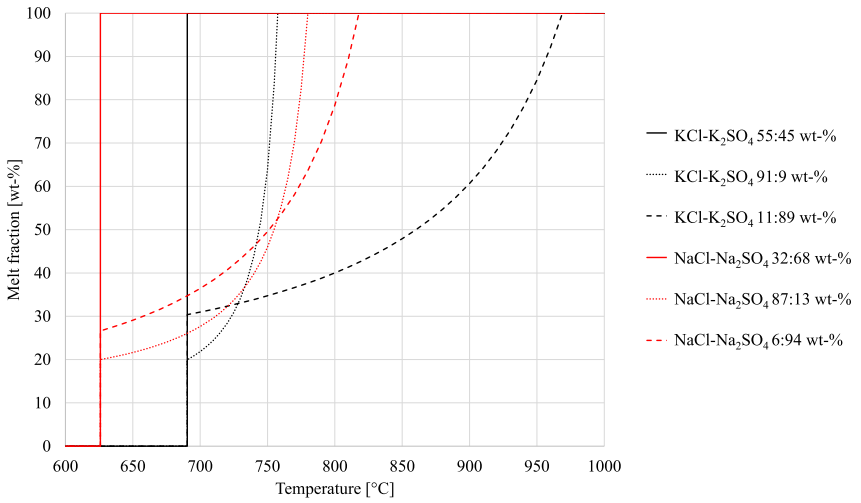

Fig. 4. Melt fraction of different NaCl–Na_2SO_4 and KCl–K_2SO_4 compositions as a function of temperature.

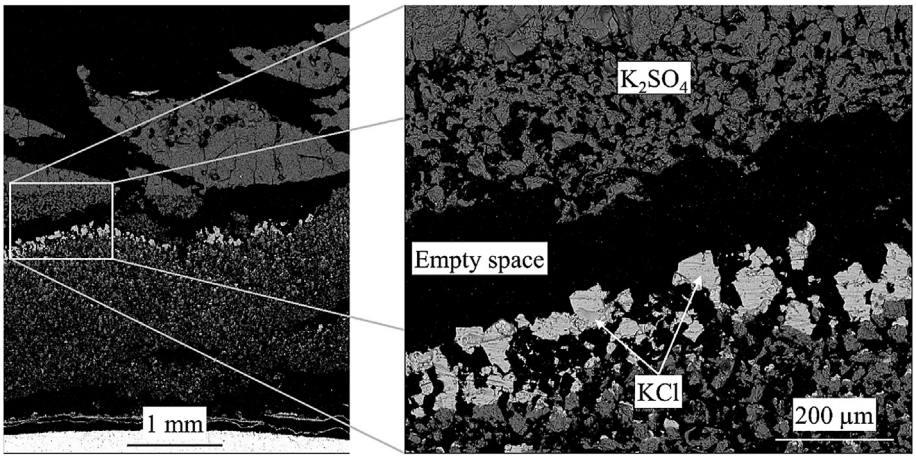

Fig. 5. On the left, a SEM image of a deposit cross-section. The deposit composition is KCl–K_2SO_4 (11:89 wt-%). On the right, a close-up on a crack within the deposit structure, showing KCl enrichment.

with the 30–53 µm particles, were not observed. The reason behind the crack formation in the experiments is not clear but thermal stresses during the heating are suspected to play a role. The formed alkali chloride layers within the cracks are thick and are therefore expected to have formed during either the heating or during the isothermal conditions. However, thermal stresses should also be present in the experiments with the 53–250 µm particles. The 30–53 µm particle deposits are expected to sinter more than the larger particle deposits, even in the subsolidus temperature regions. The sintering results in more rigid deposits. The thermal stresses experienced by the more rigid deposits could lead to crack formation within the deposit structure and explain the difference between the results from 30-53 µm and 53–250 µm deposits.

An existing alkali chloride transport model [7] was applied to predict theoretical values for the alkali chloride migration rate. The model calculates a diffusion flux according to Fick's first law of diffusion and considers that the alkali chloride evaporating from within a particle experiences a larger diffusion resistance as it needs to travel a longer path through the alkali-chloride-depleted part of the particle and that the diffusion path in the depleted part of the particle increases with time as more alkali chloride is evaporated.

The concentration gradient, which is the driving force of the diffusion, is directly proportional to the temperature gradient across the gas phase. The temperature gradient across the gas phase was estimated from the bulk temperature gradient across the porous layer, and the estimated porosity of the deposit. The temperature gradients across the porous layers in individual experiments were, from the SEM images, estimated to be 75–105 °C/mm. In the model calculations, the bulk temperature gradient was multiplied by 3.7 to account for the steeper temperature gradient across the gas phase, resulting from the differences in thermal conductivities of the air and the salt particles [7]. The diffusion of alkali chlorides increases as a linear function of the particle-to-particle temperature gradient. In addition, the saturation pressures of alkali chloride species increase exponentially as a function of local temperature, which results in an exponential increase in the diffusion rate as a function of local temperature.

For the 30–53 µm particle deposits, a particle size of 40 µm was used in the calculations, which corresponds to a particle-to-particle distance of 13.33 µm when assuming a solids fraction of 0.74 in the vertical direction. Otherwise, the same model input data applies for both the 30–53 µm and 53–250 µm size fractions. The alkali chloride layer thickness results are limited by the particle-to-

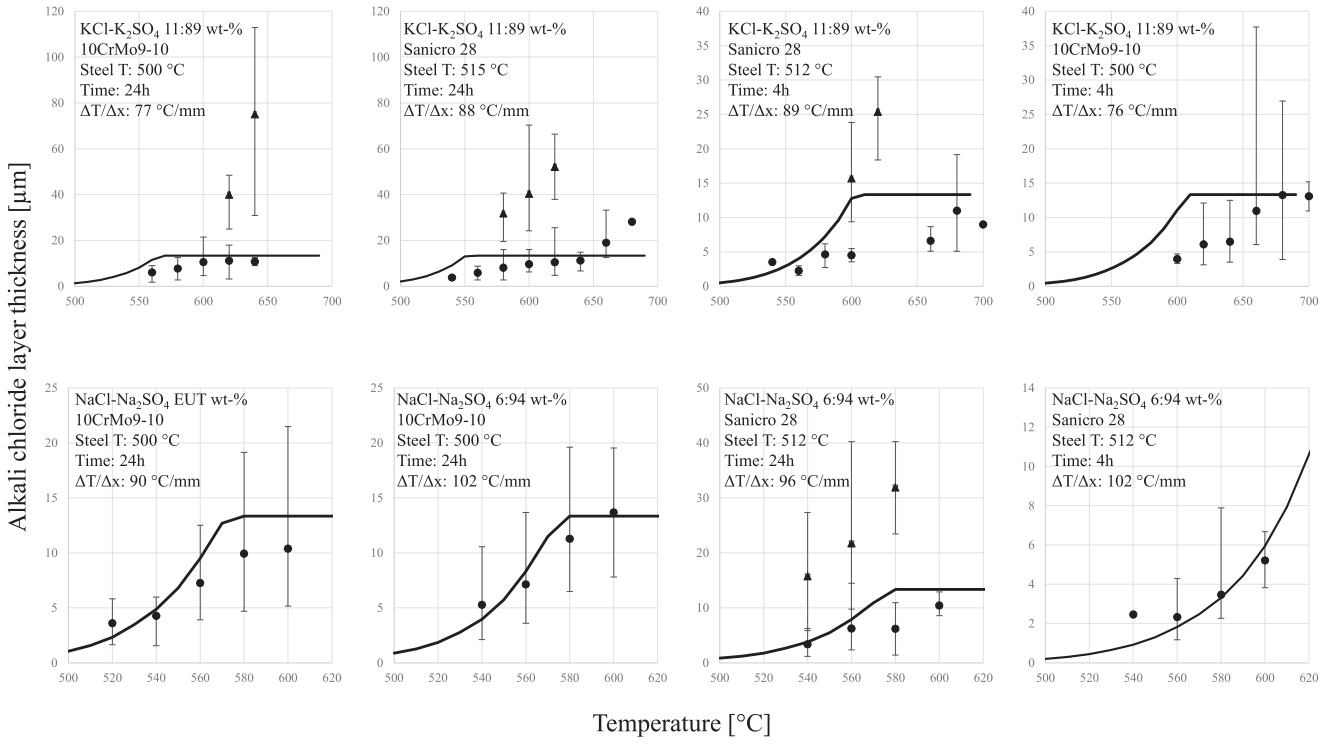

Fig. 6. Average measured alkali chloride layer thicknesses (dots) together with modeled results (continuous line) as a function of temperature in individual experiments. The dots and continuous lines show the layer thicknesses in the bulk deposit, while the triangles show the layer thickness results within the cracks. The error bars show the maximum and minimum thickness values measured in the temperature interval (20 °C) in question.

particle distance, i.e., the estimated alkali chloride layer thickness is limited to 13.33. The modeling results are shown together with the experimental data in Fig. 6.

The model predicts the alkali chloride layer thicknesses reasonably well. However, the layer thicknesses in the cracked areas were not estimated with the current model. There are a few possible explanations for the enhanced layer thicknesses within the crevices. The temperature profile is likely different over a cracked area. The temperature difference between the hotter particle surface and the colder particle surface at the edges of the cracked area is greater than between particle surfaces within a uniformly packed deposit. The saturation pressures of alkali chlorides increase exponentially as a function of temperature. In case the temperature gradient is the same, the larger temperature difference over a crack within a deposit results in a significantly greater concentration difference between particle surfaces, which drives the diffusion to occur faster. Additionally, within a crack, the alkali chloride layers have more space to grow than in the bulk deposit, where the salt particles are packed closely.

The enrichment of alkali chlorides into cracks within the laboratory-scale deposits indicates a risk of pronounced alkali chloride enrichment within deposits, which contain cracks and crevices. Structural stress to the deposit, caused e.g., by soot-blowing could lead to crack formation in deposits. In addition, enrichment of alkali chlorides could lead to a local decrease in the first melting temperature and/or increase the amount of melt present at a given location within an ash deposit. The change in the melting characteristics can in turn lead to e.g., enhanced corrosion and hardening of the deposit.

The risk of intradeposit alkali chloride enrichment increases both with higher material temperature and with steeper temperature gradients, which can be considered in boiler design. Additionally, the knowledge of the intradeposit enrichment of alkali chlorides can be considered in conjunction with temperature profile modeling. This way, the superheater tubes that experience an elevated risk of developing alkali chloride-rich deposits on the tube surface can be recognized. The tubes with elevated risk can e.g. be manufactured from advanced corrosion-resistant alloys or be coated with corrosion-resistant materials to mitigate high-temperature corrosion [17,31].

3.2. Effects H_2O and SO_2 in the gas atmosphere

The effect of the composition of the gas atmosphere on the alkali salt deposits and alkali salt-induced high-temperature corrosion was also studied. Three different gas atmospheres were used: ambient air, humid air (20% H_2O + 80% air), and humid air with SO_2 (20% H_2O + 80% air + 100 ppm SO_2). The three different atmospheres were tested with deposits consisting of either KCl or NaCl (particle size 53–250 µm). The steel temperature in all experiments was 500 °C and the exposure time was 24 h.

The experiments in ambient air showed that KCl deposits had partly melted at the top of the deposit, whereas NaCl showed no signs of melting (see Fig. 7). The difference is due to the difference in melting points, which are 770 °C for KCl and 801 °C for NaCl [25]. It is clear from the SEM images that the outer surface of the KCl deposit has experienced temperatures above its melting point, while the outer surface of the NaCl deposit has experienced temperatures below its melting point. Although signs of sintering were observed also with NaCl, they are most likely due to vaporization-condensation within the deposit, not melt formation.

In the experiments with 20% H_2O + 80% air and NaCl, the morphology of the bulk deposit was similar to the experiments in ambient air (Fig. 7). With KCl, the ambient air experiment resulted

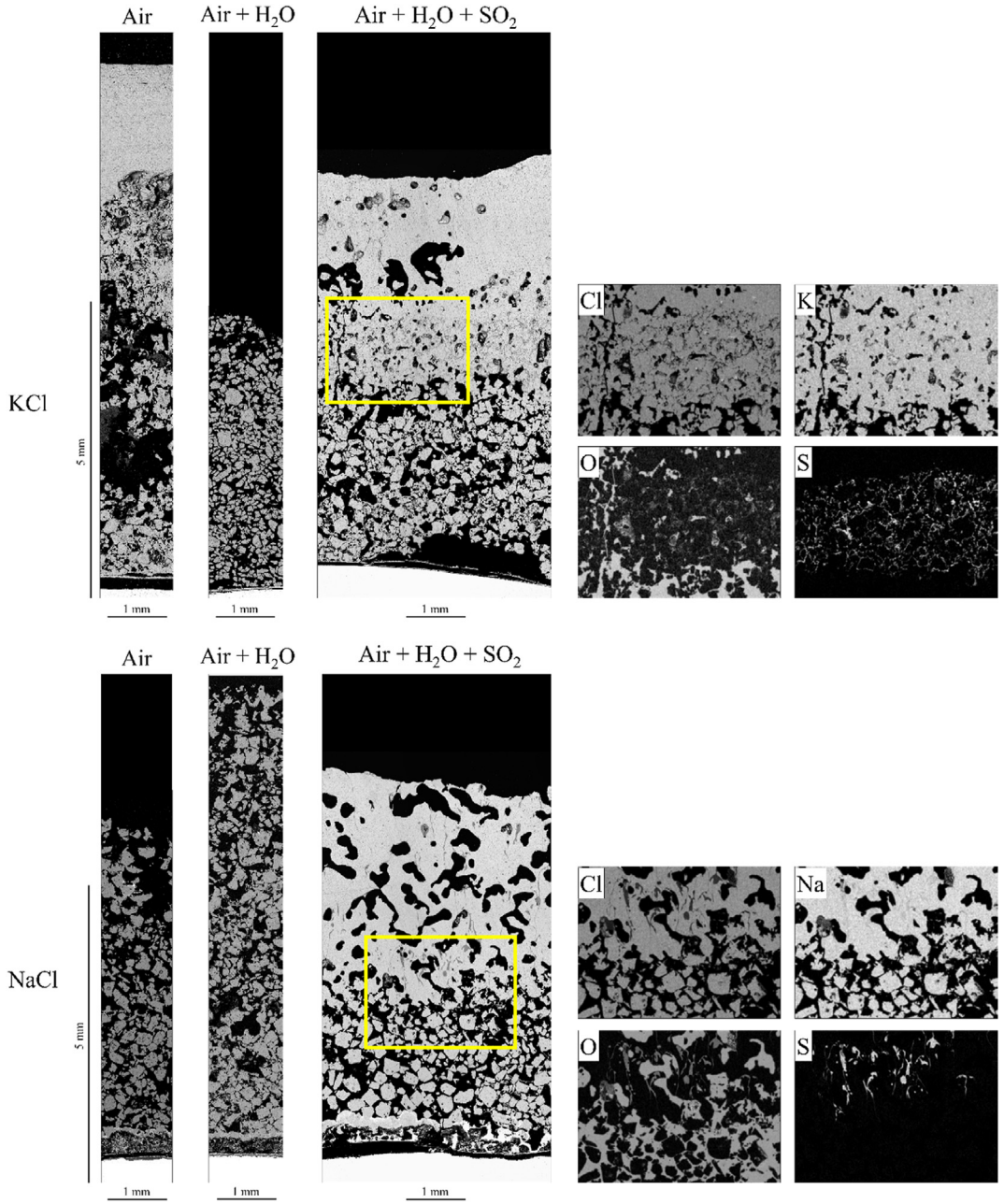

Fig. 7. SEM images of the KCl (upper row) and NaCl (lower row) deposits in different atmospheres (from left to right: ambient air, 20% H_2O + 80% air, 20% H_2O + 80% air + 100 ppm SO_2). In addition, EDX results of alkali sulfate-containing regions in the 20% H_2O + 80% air +100 ppm SO_2 atmosphere experiments are shown to the right, in which the brighter color represents a higher concentration. (For interpretation of the references to color in this figure legend, the reader is referred to the Web version of this article.)

in a sintered upper region in the deposit, which was absent in the 20% H_2O + 80% air atmosphere experiment. The reason for this difference in the upper deposit morphology is unclear. The melting point of KCl is 770 °C [25], which is slightly lower than the measured gas temperature above the deposit. The humid atmosphere KCl deposit is visibly thinner than the dry atmosphere KCl deposit, which could explain why the temperature of the deposit's outer surface is lower in the humid experiment than in the dry experiment.

With 100 ppm SO_2 in the gas, the hotter parts of the deposits were heavily sintered for both KCl and NaCl deposits (see Fig. 7). The sintered parts consisted mainly of pure NaCl or KCl but included also pockets of Na_2SO_4 or K_2SO_4 within the dense alkali chloride structure. This is similar to the earlier reported results with KCl–K_2SO_4 (96:4 M ratio) and NaCl–Na_2SO_4 (94:6 M ratio) with 53–250 μm particle size [7,10] and with the 30–53 μm particle size experiments. This shows that NaCl and KCl have been partially sulfated, leading to a lowering of the first melting temperature from 801 °C (NaCl) to 626 °C (NaCl–Na_2SO_4) for the NaCl experiments and from 770 °C (KCl) to 690 °C (KCl–K_2SO_4) for the KCl experiments [25].

KCl and NaCl are sulfated in 20% H_2O + 80% air +100 ppm SO_2 according to the bulk reaction:

$$2\,MCl\,(s,l) + H_2O\,(g) + SO_2\,(g) + \tfrac{1}{2}\,O_2\,(g) = M_2SO_4\,(s,l) + 2\,HCl\,(g) \quad (1)$$

Where M = K or Na.

The formed alkali sulfate-alkali chloride melt fills the pores between the alkali chloride particles, which leads to a liquid phase sintering of the deposit. When the melt reaches lower temperatures, the primary crystallizing phase of the mixture solidifies from the melt resulting in further densification of the deposit. When the local temperature reaches the solidus temperature of the system, the melt solidifies. The solidification of the eutectic melt results in alkali sulfate enriched areas within the alkali chloride deposits (as seen in Fig. 7). In addition, alkali sulfates were not observed below the enriched area, i.e., the densification of the upper part of the deposit protects the inner part from the reactive atmosphere.

Alkali chloride-induced corrosion can be mitigated using either co-combustion or additives, where the outcome is the sulfation of alkali chlorides [24]. Considering the temperature gradient probe results, the sulfation of alkali chlorides should occur before deposition or before the deposit has time to grow too thick. The results from the temperature gradient probe experiments show that the reactive atmosphere may not be able to reach the deposit material closest to the heat exchanger surface if the deposit morphology is dense.

Severe corrosion was observed in all cases. NaCl was more corrosive than KCl for the 10CrMo9-10, which is similar to the results reported by others [32]. Water vapor or SO_2 in the gas atmosphere did not affect the corrosion in a significant way. With NaCl, there were signs of iron chlorides present at the steel surface (Fig. 8). The iron chlorides at the steel surface were expected to have been $FeCl_2$ instead of $FeCl_3$. $FeCl_3$ needs higher Cl_2 concentrations to form compared to $FeCl_2$. In addition, solid $FeCl_3$ is stable only below 300 °C and any $FeCl_3$ that would have been formed at the steel surface would have rapidly evaporated [33]. Moving towards the deposit from the unaffected steel-corrosion front interface, the next layer was a porous layer, which was depleted of Fe compared to the bulk steel composition. The outer edge of the layer had NaCl incorporated into the layer. The layer contained high amounts of O, but as the morphology is visibly porous, the O signal likely originates from the epoxy. The Fe-depleted steel layer was followed by a thick and porous Fe-oxide layer, which also included minor amounts of NaCl. Fe-oxides were even observed within the NaCl deposit and between NaCl particles (see Fig. 8). The oxide layer of the dry exposure is shown in Fig. 8. Fig. 9 shows the oxide layers and SEM/EDX elemental maps of the other experiments with NaCl and KCl.

The corrosion behavior seems to follow the existing corrosion theories, where Cl reacts mainly with Fe and diffuses outwards as $FeCl_x$. As the $FeCl_x$ diffuses outwards and comes in contact with O_2, it reacts to Fe-oxides. The diffusion of Fe, leaves behind Fe-depleted steel, as seen in Fig. 8.

10CrMo9-10 exposed to KCl resulted in similar corrosion as with NaCl, but the Fe-oxide layer was not similarly visibly porous. In addition, the intergrown alkali chloride-metal oxide structures were significantly smaller.

With Sanicro 28 exposed to NaCl, the bulk steel was followed by a Ni-rich layer. Also, NaCl was found in this region. The Ni was likely metallic, but there was more Cl than Na, indicating a presence of chlorides of the steel metals. The following layer was mainly Cr- and Fe-oxides together with NaCl. Cr-species were enriched on the steel-facing edge of the oxide layer. The metal oxide layer was followed by the deposit material (NaCl), which was infused with Fe- and Cr-species up to the depth of several 100 μm. Similar behavior was observed for both the dry and humid atmospheres.

Sanicro 28 exposed to KCl behaved similarly as with NaCl, but less KCl-metal oxide structures were formed, and they were more local. In addition, the mixed structures also included Ni-species and the Ni-rich layer, depleted of Fe and Cr, next to the steel was thinner compared to the case with NaCl. The formation of the Cr- and Fe-oxide scales, of which the Cr-scale is closer to the steel when exposed to KCl or NaCl, is in accordance with the literature [34–36]. When exposed to KCl, the duplex oxide scale has been reported to be formed due to the outward diffusion of iron and inward diffusion of oxygen [34–36].

The humidity has been reported to affect the high-temperature corrosion of chromia-forming alloys [37]. However, only minor differences between the dry and humid conditions were observed

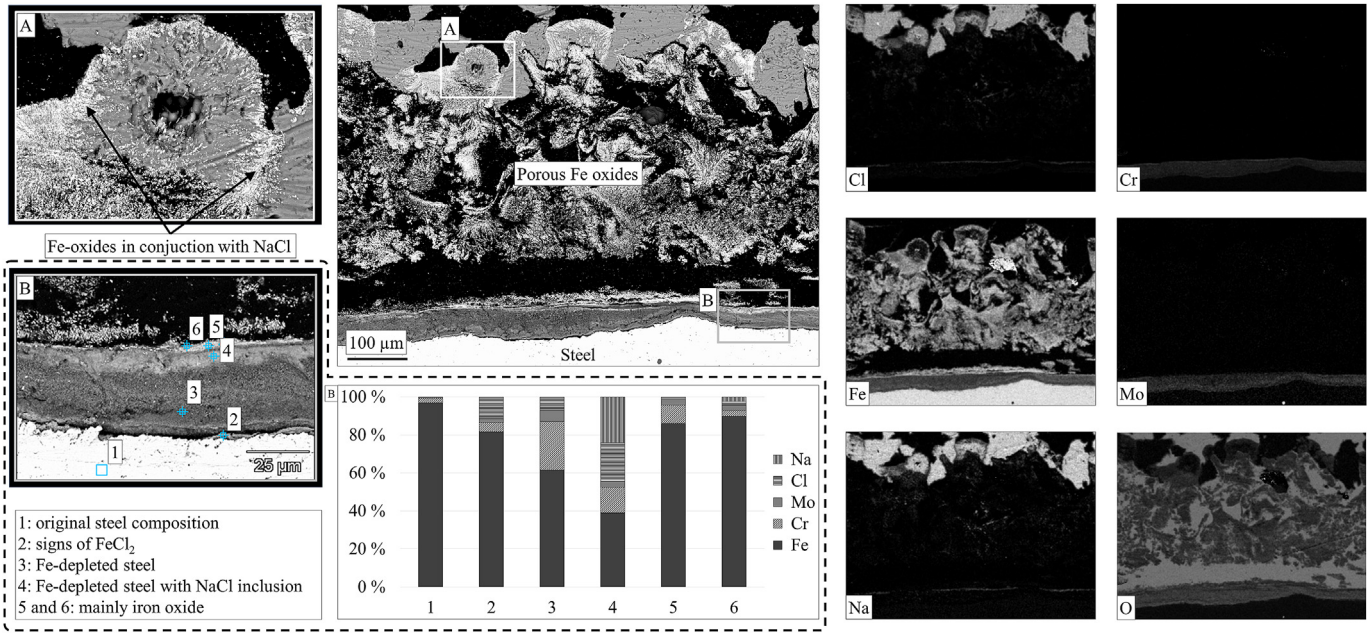

Fig. 8. The corrosion product layer of 10CrMo9-10 steel exposed to NaCl for 24 h in the temperature gradient furnace in an ambient atmosphere. The steel temperature was 510 °C and the furnace temperature ~800 °C. On the left, a close-up on the deposit with iron oxide infused NaCl and a close-up on the corrosion-front with EDX-point analysis (molar ratio with oxygen excluded). On the right, EDX elemental analysis map of the area.

Fig. 9. SEM images and EDX elemental maps of corrosion fronts of 10CrMo9-10 and Sanicro 28 steels with NaCl and KCl as deposit materials, exposed to different gas-atmospheres for 24h.

in the present temperature gradient experiments.

3.3. Effect of exposure time

The results from the 168 h experiments with the eutectic NaCl–Na_2SO_4 (32:68 wt-%) and KCl–K_2SO_4 (56:44 wt-%) mixtures showed similar deposit structures as for the published 4–72 h tests [7,10], except for the test with eutectic NaCl–Na_2SO_4 on the Sanicro 28 steel. The eutectic NaCl–Na_2SO_4 salt deposit was dense and completely sintered down to the metal oxide surface. The steel ring temperature was ~517 °C. The deposit is shown in Fig. 10 together with results from a 24 h experiment with the same deposit composition and steel temperature.

The eutectic NaCl–Na_2SO_4 on the Sanicro 28 steel also included Fe- and Ni-oxides on top of the deposit, facing the hot furnace air. The first melting temperature of the original deposit (626 °C) is significantly higher than the steel ring temperature. However, the completely sintered structure implies that there has been melt formation throughout the deposit during the experiment.

A plausible explanation for the melt formation below 626 °C is the formation of Fe- and Ni-chlorides at the metal surface. The presence of the corrosion products (iron and nickel oxides) within and above the dense deposit structure also supports this hypothesis. The formation of Fe- and Ni-chlorides at the steel surface would lead to a reaction with the deposit material, resulting in a decrease of the first melting temperature of the deposit and subsequently in the dissolving of the Fe-and Ni-chlorides into the molten phase together with the deposit material. For example, the $FeCl_2$–NaCl–$NiCl_2$ system forms a melt already at temperatures below 400 °C [38]. Indications for such behavior were also shown in

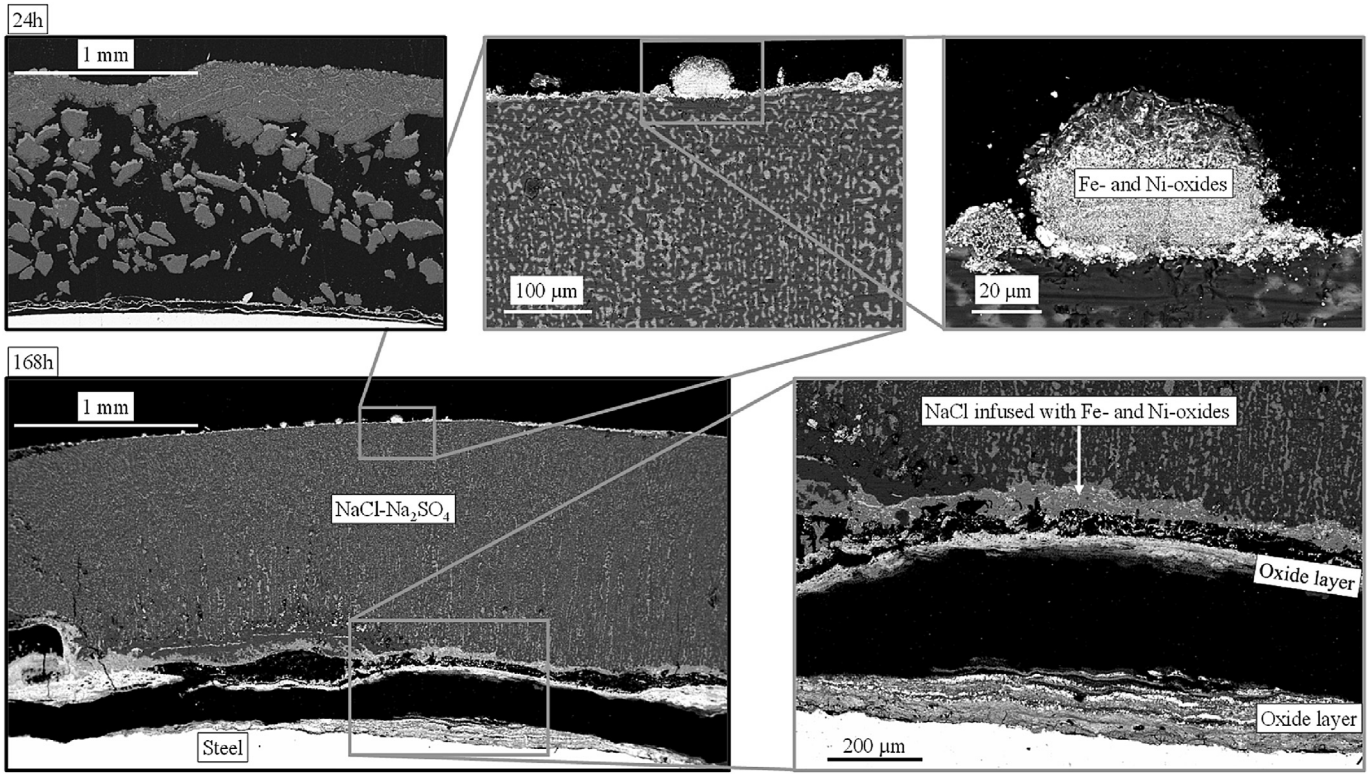

Fig. 10. The eutectic NaCl–Na_2SO_4 deposits after 24 h [7] and 168 h exposures in the temperature gradient furnace showing the densification of the deposit as an effect of exposure time. Close-up on the oxide scale and the outer edge of the deposit showing the Fe- and Ni-oxides.

the 24 h experiments with NaCl as the deposit material (see Figs. 8 and 9). Some similar effects have been reported also earlier [6,8]. With high enough partial pressure of O_2, the Fe- and Ni-chlorides oxidize into Fe- and Ni-oxides. The sintering throughout the deposit is expected to be a process, which takes a relatively long time.

It has been shown that Fe- and Ni-chlorides are formed when the steel is exposed to alkali chlorides at high temperatures [22,39,40]. Additionally, $CrCl_2$ and $CrCl_3$ could in theory be formed [40], but no Cr-oxides were observed at the outer surface or within the deposit. The Fe- and Ni-chlorides in question are stable only at very low O_2 partial pressures. Such conditions are locally present at the steel surface. The formation of Cr-chlorides is not expected as it requires extremely low O_2 partial pressures. Even if Cr-chlorides were to form, they react to Cr-oxides at a lower O_2 partial pressure than the Fe- and Ni-chlorides [40,41].

The formation of a melt close to the metal surface was observed also in the shorter experiments, but not to the same extent. In addition, in one of the experiments with small particles (30–53 µm) with a eutectic NaCl–Na_2SO_4 deposit, corrosion products were observed within the dense deposit structure.

The presence of Fe- and Ni-oxides at the outer surface of the NaCl–Na_2SO_4 deposit in the 168 h experiment can be explained by a temperature gradient zone melting (TGZM) mechanism [7,42]. Some Fe- and Ni-oxides were observed within the deposit together with NaCl. In addition, the NaCl–Na_2SO_4 deposit structure (Fig. 10) contained channels in the same direction as the temperature gradient, which supports the TGZM mechanism hypothesis.

The melting behavior of the $FeCl_2$–NaCl–$NiCl_2$ system was considered using thermodynamic modeling to validate the TGZM as the responsible mechanism. The $FeCl_2$–NaCl–$NiCl_2$ system was chosen because the Fe- and Ni-species found close to the steel surface and at the deposit surface were in conjunction with NaCl. Sulfate-species were not included in the thermodynamic calculations. A finite amount of discrete compositions was considered. The amounts of $FeCl_2$ and $NiCl_2$ in the compositions were low and the considered compositions are listed in Table 4.

The melting behavior of the modeled compositions is shown in Fig. 11. All mixtures form a first melt at 377 °C, which is the eutectic temperature of the $FeCl_2$–NaCl–$NiCl_2$ system [38]. The amount of melt at the solidus temperature increases nearly linearly as a function of the Fe/(Fe + Na) ratio. The temperature and composition of the eutectic point of the binary $FeCl_2$–NaCl system are 378 °C at 43.8:56.2 mol fraction. The temperature and composition of the eutectic point of the ternary $FeCl_2$–NaCl–$NiCl_2$ system are 377 °C at 43.0:56.2:0.8 mol fraction [38].

$NiCl_2$ is gradually included in the melt phase. As more NaCl is dissolved into the melt phase with $FeCl_2$, also more $NiCl_2$ is incorporated into the melt phase. The ratio of $NiCl_2$ possible to incorporate into the melt is a function of temperature as shown in Fig. 11. The ratio of Ni in the melt phase initially increases with increasing temperature until all the Ni is incorporated into the melt phase. After that, the amount of Ni in the melt phase decreases as the temperature increases and more Na is incorporated into the melt and the Ni concentration becomes diluted. The change in the Fe:Ni ratio changes the composition of the melt phase as seen in Fig. 11. The compositions 5.4:90:4.6 and 0.54:99:0.46 (Fe:Na:Ni molar ratio) have the same Fe:Ni ratio as the Sanicro 28 steel. The Ni concentration in the melt for those compositions starts to decrease as a function of temperature when the temperature is higher than 540 °C.

In all the cases considered, the ratio of Fe in the melt decreases as the temperature increases. The concentration gradient in the melt phase leads to a potential difference across the melt, in the direction of the temperature gradient. The potential difference

Table 4
The compositions considered for the $FeCl_2$–NaCl–$NiCl_2$ system.

Composition ID (Fe:Na:Ni)	Composition [mole fraction]			Melt formation [°C]	Melt amount at solidus [wt-%]
	$FeCl_2$	NaCl	$NiCl_2$		
5:90:5	0.05	0.9	0.05	377	15.7
1:90:9	0.01	0.9	0.09	377	3.0
9:90:1	0.09	0.9	0.01	377	28.4
2.5:90:7.5	0.025	0.9	0.075	377	7.7
7.5:90:2.5	0.075	0.9	0.025	377	23.6
5.4:90:4.6	0.054	0.9	0.046	377	16.9
0.54:99:0.46	0.0054	0.99	0.0046	377	1.8

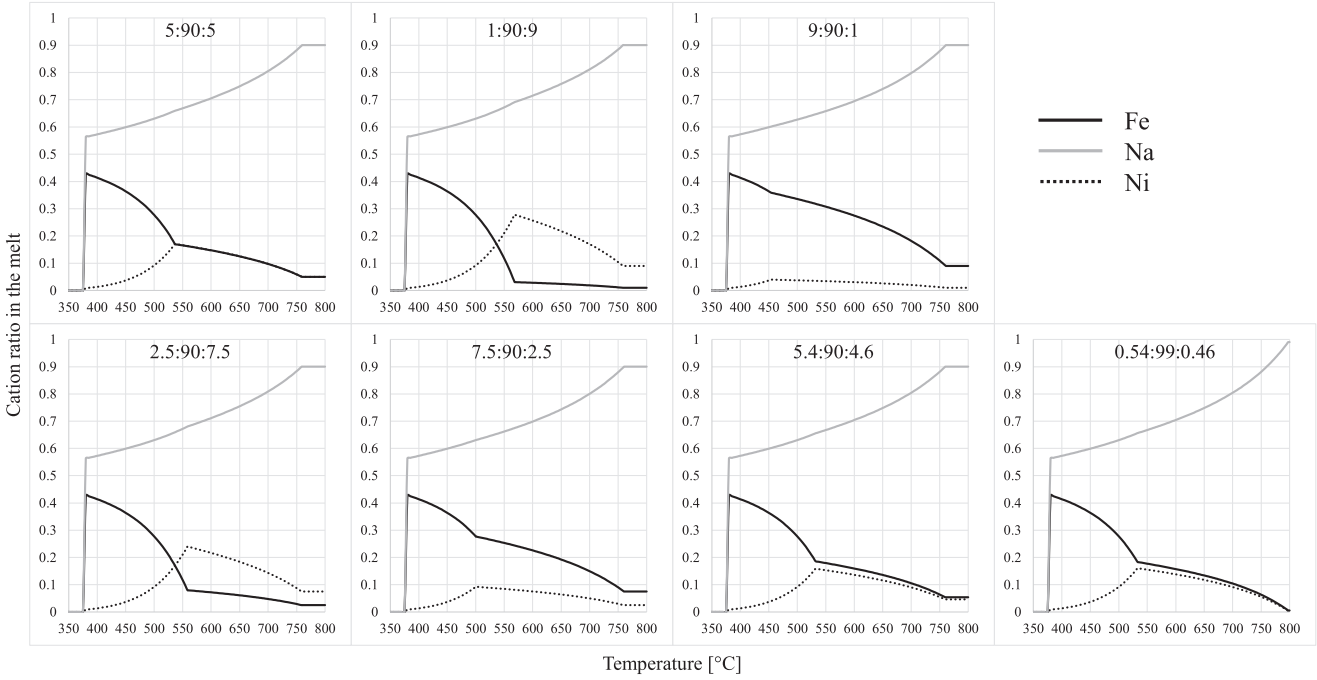

Fig. 11. The calculated composition of the melt with different Fe:Na:Ni ratios. The figures show the cation ratio of the melt as a function of temperature.

results in the diffusion of the Fe towards the hotter temperature. Similar behavior occurs for Ni in temperatures where all the Ni has been incorporated into the melt phase. In addition, Na diffuses towards colder temperatures to balance the potential difference.

The diffusion of Fe (and Ni) towards the hotter temperature and Na towards the colder temperature results in supersaturation of Na in the colder temperatures, which results in precipitation of the primary crystallizing phase (NaCl) from the melt. In the hotter temperatures, supersaturation of Fe results in more NaCl to be incorporated into the melt phase, i.e., an increase in the amount of melt in the hotter temperature region. The mechanism continues until the Fe- and Ni-chlorides come into contact with high enough O_2 partial pressure and oxidize into metal oxides. In a completely dense system, such as the NaCl–Na_2SO_4 deposit after 168 h exposure, the oxidation takes place at the outer surface of the deposit.

The results from the 168 h experiments show that the formation of compact and dense deposits can induce faster corrosion kinetics than initially expected. There is an implication for the need for more frequent soot-blowing in regions where such dense deposits are likely to occur. In addition to the implied risk for faster corrosion kinetics, dense deposits also have higher adhesion strength, which makes them harder to remove [30].

4. Conclusions

The main morphological changes in all of the experiments were connected to the formation of liquid phases within the deposits. The formation of the liquid phase leads to liquid phase sintering. Smaller particles and higher amounts of melt result in faster and more extensive sintering of the deposits. Additionally, species included in the molten phase were observed to enrich in regions within the deposits, which during the temperature gradient exposure experienced temperatures corresponding to the solidus temperature of the deposit material. The molten phases form in regions with higher temperatures and due to capillary forces move towards the colder temperatures and solidify as temperature decreases.

The dry and humid atmospheres did not result in significant differences between KCl and NaCl deposits. With the addition of SO_2 into the humid atmosphere, some of the alkali chlorides reacted to alkali sulfates. The SO_2 reacted with the outer layer of the deposit. The reaction and the subsequent melt formation between the alkali chlorides and alkali sulfates lead to liquid phase sintering of the deposit. This results in a dense deposit structure, which cannot in practice be penetrated by the SO_2, and therefore the inner deposit remained unaffected by the SO_2 in the atmosphere.

Smaller particle deposits had a slower enrichment of alkali chlorides toward the steel surface, which could indicate a lower corrosion risk. Cracks within the deposit structure may enhance the alkali chloride enrichment thus increasing the risk for corrosion, especially if the cracks reach the steel surface. Large cracks in the deposit structure were present only with the smaller particle size deposits.

The corrosion in the presence of a temperature gradient was observed severe for both 10CrMo9-10 and Sanicro 28 when exposed to the alkali chloride-containing salt mixtures.

One-week exposure to a $NaCl-Na_2SO_4$ deposit was observed to result in a completely dense deposit structure, with corrosion products also at the outer edge of the deposit. Only one out of four of the 168 h experiments resulted in a completely dense deposit, which implies that the overall densification mechanism is slow, and even with long exposures does not always occur. The deposit densification process is due to the formation of iron and nickel chlorides at the steel surface. The formation of iron and nickel chlorides results in melt formation, which results in the densification of the deposit. Additionally, the iron and nickel chlorides migrate towards the deposit outer surface due to the TGZM mechanism.

Credit author statement

Jonne Niemi: Conceptualization, Methodology, Software, Formal analysis, Investigation, Data curation, Writing – original draft, Writing – review & editing, Visualization. Markus Engblom: Conceptualization, Methodology, Writing – review & editing. Tor Laurén: Investigation. Patrik Yrjas: Writing – review & editing, Project administration, Funding acquisition. Juho Lehmusto: Writing – review & editing. Mikko Hupa: Conceptualization, Writing – review & editing, Supervision, Funding acquisition. Daniel Lindberg: Conceptualization, Methodology, Software, Writing – review & editing, Supervision, Project administration, Funding acquisition.

Declaration of competing interest

The authors declare that they have no known competing financial interests or personal relationships that could have appeared to influence the work reported in this paper.

Acknowledgments

This work was conducted within the Academy of Finland projects “Understanding the dynamics of intradeposit chemistry and morphology for control of corrosion in high temperature processes” (Decision 310266) and “Behavior and properties of molten ash in biomass and waste combustion” (Decision 266384). The work has been partly carried out within CLIFF (2014–2017) as part of the activities of the Åbo Akademi University Johan Gadolin Process Chemistry Centre. Other research partners were VTT Technical Research Centre of Finland Ltd, Lappeenranta University of Technology, Aalto University, and Tampere University of Technology. Support from the National Technology Agency of Finland (Tekes), Andritz Oy, Valmet Technologies Oy, Sumitomo SHI FW, UPM-Kymmene Oyj, Clyde Bergemann GmbH, International Paper Inc., and Top Analytica Oy Ab is gratefully acknowledged. The authors would like to thank Linus Silvander for operating the SEM apparatus and Jaana Paananen for her help with the experimental setup and sample preparation.

References

[1] Hupa M, Karlström O, Vainio E. Biomass combustion technology development - it is all about chemical details. Proc Combust Inst 2017;36:113–34. https://doi.org/10.1016/j.proci.2016.06.152.
[2] Zbogar A, Frandsen F, Jensen PA, Glarborg P. Shedding of ash deposits. Prog Energy Combust Sci 2009;35:31–56. https://doi.org/10.1016/j.pecs.2008.07.001.
[3] Brossard JM, Diop I, Chaucherie X, Nicol F, Rapin C, Vilasi M. Superheater fireside corrosion mechanisms in MSWI plants: lab-scale study and on-site results. Mater Corros 2011;62:543–8. https://doi.org/10.1002/maco.201005849.
[4] Schaal E, David N, Panteix PJ, Rapin C, Vilasi M, Mathieu S, et al. Effect of zinc chloride in ash in oxidation kinetics of Ni-based and Fe-based alloys. Oxid Met 2016;85:547–63. https://doi.org/10.1007/s11085-016-9612-5.
[5] Kawahara Y. Evaluation of high-temperature corrosion life using temperature gradient corrosion test with thermal cycle component in waste combustion environments. Mater Corros 2006;57:60–72. https://doi.org/10.1002/maco.200503895.
[6] Lagerbom J, Lepistö T, Backman R, Hupa M. Behavior of alkaline sulfate-chloride salts in temperature gradient corrosion test furnace. VTT Symp, vol. 215, n.d., p. 541–551.
[7] Niemi J, Lindberg D, Engblom M, Hupa M. Simultaneous melt and vapor induced ash deposit aging mechanisms – mathematical model and experimental observations. Chem Eng Sci 2017;173:196–207. https://doi.org/10.1016/j.ces.2017.07.041.
[8] Niemi J, Balint R, Engblom M, Lehmusto J, Lindberg D. Temperature-gradient-driven aging mechanisms in alkali-bromide- and sulfate-containing ash deposits. Energy Fuels 2019;33:5883–92. https://doi.org/10.1021/acs.energyfuels.8b04199.
[9] Niemi J, Lindberg D, Engblom M, Tran H. A fundamental study on the change in composition of fireside deposits with time in kraft recovery boilers. J Sci Technol For Prod Process 2018;7:45–52.
[10] Lindberg D, Niemi J, Engblom M, Yrjas P, Laurén T, Hupa M. Effect of temperature gradient on composition and morphology of synthetic chlorine-containing biomass boiler deposits. Fuel Process Technol 2016;141:285–98. https://doi.org/10.1016/j.fuproc.2015.10.011.
[11] Niemi J, Kinnunen H, Lindberg D, Enestam S. Interactions of $PbCl_2$ with alkali salts in ash deposits and effects on boiler corrosion. Energy Fuels 2018;32:8519–29. https://doi.org/10.1021/acs.energyfuels.8b01722.
[12] Kinnunen H, Lindberg D, Laurén T, Uusitalo M, Bankiewicz D, Enestam S, et al. High-temperature corrosion due to lead chloride mixtures simulating fireside deposits in boilers firing recycled wood. Fuel Process Technol 2017;167:306–13. https://doi.org/10.1016/j.fuproc.2017.07.017.
[13] Liu Y, Fan W, Zhang X, Wu X. High-temperature corrosion properties of boiler steels under a simulated high-chlorine coal-firing atmosphere. Energy Fuels 2017;31:4391–9. https://doi.org/10.1021/acs.energyfuels.6b02755.
[14] Brossard JM, Lebel F, Rapin C, Marêché JF, Chaucherie X, Nicol F, et al. Lab-scale study on fireside superheaters corrosion in MSWI plants. Proc. 17th Annu. North Am. Waste to Energy Conf. NAWTEC17 2009:63–9. https://doi.org/10.1115/NAWTEC17-2339.
[15] Montgomery M, Jensen SA, Borg U, Biede O, Vilhelmsen T. Experiences with high temperature corrosion at straw-firing power plants in Denmark. Mater Corros 2011;62:593–605. https://doi.org/10.1002/maco.201005856.
[16] Kleinhans U, Wieland C, Frandsen FJ, Spliethoff H. Ash formation and deposition in coal and biomass fired combustion systems: progress and challenges in the field of ash particle sticking and rebound behavior. Prog Energy Combust Sci 2018;68:65–168. https://doi.org/10.1016/j.pecs.2018.02.001.
[17] Wu D, Dahl KV, Madsen JL, Christiansen TL, Montgomery M, Hald J. Effects of different fuel specifications and operation conditions on the performance of coated and uncoated superheater tubes in two different biomass-fired boilers. ACS Appl Energy Mater 2018;1:1463–75.
[18] Balint R, Engblom M, Niemi J, Silva da Costa D, Lindberg D, Yrjas P, et al. Temperature gradient induced changes within superheater ash deposits high in chlorine. Energy 2021:120439. https://doi.org/10.1016/j.energy.2021.120439.
[19] Tran H. Upper furnace deposition and plugging. In: Adams TN, editor. Kraft recover. Boil. Tappi Press; 1997.
[20] Michelsen HP, Frandsen F, Dam-Johansen K, Larsen OH. Deposition and high temperature corrosion in a 10 MW straw fired boiler. Fuel Process Technol 1998;54:95–108. https://doi.org/10.1016/S0378-3820(97)00062-3.
[21] Nielsen HP, Frandsen FJ, Dam-Johansen K, Baxter LL. The implications of chlorine-associated corrosion on the operation of biomass-fired boilers. Prog Energy Combust Sci 2000;26:283–98.
[22] Persson K, Broström M, Carlsson J, Nordin A, Backman R. High temperature corrosion in a 65 MW waste to energy plant. Fuel Process Technol 2007;88:1178–82. https://doi.org/10.1016/j.fuproc.2007.06.031.
[23] Vainio E, Brink A, Hupa M, Vesala H, Kajolinna T. Fate of fuel nitrogen in the furnace of an industrial bubbling fluidized bed boiler during combustion of biomass fuel mixtures. Energy Fuels 2012;26:94–101. https://doi.org/10.1021/ef201145j. American Chemical Society.
[24] Kassman H, Pettersson J, Steenari BM, Åmand LE. Two strategies to reduce gaseous KCl and chlorine in deposits during biomass combustion - injection of ammonium sulphate and co-combustion with peat. Fuel process. Technol.,

vol. 105. Elsevier; 2013. p. 170–80. https://doi.org/10.1016/j.fuproc.2011.06.025.
[25] Bale CW, Belisle E, Chartrand P, Decterov SA, Eriksson G, Gheribi AE, et al. FactSage thermochemical software and databases, 2010-2016. Calphad Comput Coupling Phase Diagrams Thermochem 2016;54:35–53. https://doi.org/10.1016/j.calphad.2016.05.002.
[26] Jensen PA, Frandsen FJ, Hansen J, Dam-Johansen K, Henrisken N, Hörlyck S. SEM investigation of superheater deposits from biomass-fired boilers. Energy Fuels 2004;18:378–84. https://doi.org/10.1021/ef030097l.
[27] Hansen LA, Nielsen HP, Frandsen FJ, Dam-Johansen K, Hørlyck S, Karlsson A. Influence of deposit formation on corrosion at a straw-fired boiler. Fuel Process Technol 2000;64:189–209. https://doi.org/10.1016/S0378-3820(00)00063-1.
[28] German RM, Suri P, Park SJ. Review: liquid phase sintering. J Mater Sci 2009;44:1–39. https://doi.org/10.1007/s10853-008-3008-0.
[29] Frederick WJ, Vakkilainen EK. Sintering and structure development in alkali metal salt deposits formed in kraft recovery boilers. Energy Fuels 2003;17:1501–9. https://doi.org/10.1021/ef034012s.
[30] Laxminarayan Y, Nair AB, Jensen PA, Wu H, Frandsen FJ, Sander B, et al. Tensile adhesion strength of biomass ash deposits: effect of the temperature gradient and ash chemistry. Energy Fuels 2018;32:4432–41. https://doi.org/10.1021/acs.energyfuels.7b03114.
[31] Ma W, Wenga T, Frandsen FJ, Yan B, Chen G. The fate of chlorine during MSW incineration: vaporization, transformation, deposition, corrosion and remedies. Prog Energy Combust Sci 2020;76:100789. https://doi.org/10.1016/j.pecs.2019.100789.
[32] Enestam S, Bankiewicz D, Tuiremo J, Mäkelä K, Hupa M. Are NaCl and KCl equally corrosive on superheater materials of steam boilers? Fuel 2013;104:294–306. https://doi.org/10.1016/j.fuel.2012.07.020.
[33] Dudziak T, Jura K, Rutkowska J. Chlorine corrosion degradation of low alloyed ferritic steels in temperature range 450–550 °C. Oxid Met 2016;85:647–64. https://doi.org/10.1007/s11085-016-9617-0.
[34] Pettersson C, Jonsson T, Proff C, Halvarsson M, Svensson JE, Johansson LG. High temperature oxidation of the austenitic (35Fe27Cr31Ni) alloy sanicro 28 in O 2 + H 2O environment. Oxid Met 2010;74:93–111. https://doi.org/10.1007/s11085-010-9199-1.
[35] Lehmusto J, Bergelin M, Sui J, Juhanoja J, Skrifvars BJ, Yrjas P. Applicability of ToF-SIMS and stable oxygen isotopes in KCl-induced corrosion studies at high temperatures. Corrosion Sci 2017;125:1–11. https://doi.org/10.1016/j.corsci.2017.05.022.
[36] Sui J, Lehmusto J, Bergelin M, Hupa L. Initial oxidation mechanisms of stainless steel Sanicro 28 (35Fe27Cr31Ni) exposed to KCl, NaCl, and K 2 CO 3 under dry and humid conditions at 535 °C. Corrosion Sci 2019;155:29–45. https://doi.org/10.1016/j.corsci.2019.04.010.
[37] Sadeghi E, Markocsan N, Joshi S. Advances in corrosion-resistant thermal spray coatings for renewable energy power plants: Part II—effect of environment and outlook. J Therm Spray Technol 2019;28:1789–850. https://doi.org/10.1007/s11666-019-00939-0.
[38] Robelin C, Chartrand P, Pelton AD. Thermodynamic evaluation and optimization of the (NaCl + KCl + MgCl 2 + CaCl2 + MnCl2 + FeCl2 + CoCl2 + NiCl2) system. J Chem Thermodyn 2004. https://doi.org/10.1016/j.jct.2004.05.005.
[39] Grabke HJ, Reese E, Spiegel M. The effects of chlorides, hydrogen chloride, and sulfur dioxide in the oxidation of steels below deposits. Corrosion Sci 1995;37:1023–43. https://doi.org/10.1016/0010-938x(95)00011-8.
[40] Zahs A, Spiegel M, Grabke HJ. Chloridation and oxidation of iron, chromium, nickel and their alloys in chloridizing and oxidizing atmospheres at 400-700°C. Corrosion Sci 2000;42:1093–122. https://doi.org/10.1016/S0010-938X(99)00142-0.
[41] Pradhan D, Shankar Mahobia G, Chattopadhyay K, Singh V. Salt induced corrosion behaviour of superalloy IN718. Mater Today Proc 2018;5:7047–54. https://doi.org/10.1016/J.MATPR.2017.11.368.
[42] Pfann WG. Temperature gradient zone melting. Trans AIME 1955;203:961–4.